Journal of Environmental Chemical Engineering 12 (2024) 114312

Contents lists available at ScienceDirect

Journal of Environmental Chemical Engineering

journal homepage: www.elsevier.com/locate/jece

Tailoring of Zinc Oxide-based microstructures to efficiently promote piezocatalytic water oxidation and oxygen production

Simona Bettini [a,e,1], Rosanna Pagano [a,1], Donato Valli [b], Michela Ottolini [a], Sudipto Pal [c], Johan Hofkens [b], Maarten Roeffaers [d], Gabriele Giancane [e,f,*], Ludovico Valli [a,f]

[a] Dipartimento di Scienze e Tecnologie Biologiche e Ambientali, Universita` del Salento, Via Monteroni, Lecce I-73100, Italy
[b] Department of Chemistry, KU Leuven, Celestijnenlaan 200F, Heverlee 3001, Belgium
[c] Dipartimento di Ingegneria dell'Innovazione, Università del Salento, Via Monteroni, Lecce I-73100, Italy
[d] cMACS, Department of Microbial and Molecular Systems, KU Leuven, Celestijnenlaan 200F, Heverlee 3001, Belgium
[e] Dipartimento di Beni Culturali, Universita` del Salento, Via Dalmazio Birago, 64, Lecce I-73100, Italy
[f] Consorzio Interuniversitario Nazionale per la Scienza e la Tecnologia dei Materiali, INSTM, Via G. Giusti, Firenze I-50121, Italy

ARTICLE INFO

Keywords:
Zinc oxide
Piezoelectric effect
Piezocatalysis
Oxygen evolution
Oxidative water splitting

ABSTRACT

Two zinc oxide (ZnO) nanomaterials, exhibiting distinct morphologies, were synthesized in wurtzite phase through chemical precipitation. The elongated shape rod-like ZnO (R-ZnO) exhibited more pronounced piezoelectric characteristics compared to the more compact flower-like ZnO (F-ZnO). Detailed characterization including piezoforce microscopy, finite element simulation, revealed that the remarkable piezoelectric properties of R-ZnO are due to its strongly anisotropic structure, enabling significant mechanical deformation under ultrasound in aqueous suspension. The piezocatalytical degradation of these materials was assessed using methylene blue as a test organic dye across various ultrasound frequencies, with R-ZnO consistently outperforming F-ZnO. This highlighted the impact of structural deformability on piezocatalytic efficiency. Additionally, the capability of R-ZnO to facilitate oxygen evolution from water through ultrasound-induced stress was explored in an oxygen-free environment. Our findings demonstrate that R-ZnO can effectively catalyze water oxidation and produce oxygen directly, showcasing its potential as a standalone catalyst for environmental remediation and sustainable chemical processes.

1. Introduction

Among the challenges of environmental sustainability, the quest for innovative catalytic systems capable of supporting energy conversion processes is critical [1]. In this context, multifunctional materials are gaining attention for their ability to catalyse essential chemical reactions such as water oxidation (WO) and water splitting (WS) reactions [2,3]. Specifically, water splitting encompasses two critical half-reactions:

$$\text{Hydrogen Evolution Reaction(HER)} \quad 4H^+ + 4e^- \rightarrow 2H_2 (E^\circ = 0V) \tag{1}$$

$$\text{Oxygen Evolution Reaction(OER)} \quad 2H_2O + 4h^+ \rightarrow O_2 + 4H^+ (E^\circ = 1.23V) \tag{2}$$

Various methods have been developed to achieve WS including photocatalytic, electrochemical and photoelectrochemical [4,5]. The photocatalytic process involves exciton formation when semiconducting catalysts absorb photons [6]. Crucially, after exciton formation, the excited charge carriers must separate and migrate to the catalyst's surface to initiate the chemical reactions. This step is vital as it influences the efficiency of the photocatalysis by determining how effectively these carriers contribute to the reaction processes. In electrocatalysis electrons and holes are supplied from an external source rather than generated internally through photon absorption [7,8].

While electrocatalysis harnesses external electrical inputs to control electron and hole movements effectively, another innovative approach involves the use of mechanical energy to generate these essential charge carriers. This method taps into the unique properties of piezoelectric materials, which can convert mechanical stress directly into electrical energy [9]. Piezocatalysis utilizes the displacement of free charge

* Corresponding author at: Dipartimento di Beni Culturali, Universita` del Salento, Via Dalmazio Birago, 64, Lecce I-73100, Italy.
E-mail address: gabriele.giancane@unisalento.it (G. Giancane).
[1] These authors equally contributed.

https://doi.org/10.1016/j.jece.2024.114312
Received 18 June 2024; Received in revised form 29 August 2024; Accepted 29 September 2024
Available online 30 September 2024

carriers generated by the formation of a dipole moment within the catalyst's structure upon the application of mechanical stress [10]. This capability is deeply connected to the field of green and sustainable chemistry, as piezoelectric materials can harvest clean vibration energy from ambient sources such as wind, waves, and sound energy [11–14].

The working principle involves the direct piezoelectric effect, where mechanical stress, such as ultrasound stimulation [15], generates an electric potential. This bias can catalyse key redox processes central to WS and WO. Such processes facilitate the production of green energy vectors [16,17], and of reactive oxygen species (ROS) like ·OH and $\cdot O_2^-$, crucial for oxidative processes in water remediation [18]. The key redox reactions, including Eqs.1 and 2, are:

$$O_2 + e^- \rightarrow \cdot O_2^- (E^\circ = -0.16V) \quad (3)$$

$$\cdot O_2^- + 2H^+ + e^- \rightarrow H_2O_2 (E^\circ = 0.89\ V) \quad (4)$$

$$H_2O_2 + e^- + H^+ \rightarrow \cdot OH + H_2O (E^\circ = 0.38\ V) \quad (5)$$

$$O_2 + 2e^- + 2H^+ \rightarrow H_2O_2 (E^\circ = 2.38\ V) \quad (6)$$

$$H_2O + h^+ \rightarrow \cdot OH + H^+ (E^\circ = 0.28\ V) \quad (7)$$

Among potential piezocatalysts are materials like ZnO, MoS_2, $Cu_3B_2O_6$, $BaTiO_3$, $Pb(Zr_{0.5}2Ti_{0.48})O_3$, $BiFeO_3$, $Bi_2Fe_4O_9$, $NaNbO_3$, $KNbO_3$, $Na_{0.5}K_{0.5}NbO_3$, Bi_4NbO_8X (X = Cl/Br), $BiOIO_3$, and UiO-66-NH_2(Hf/Zr) [19]. However, challenges remain, such as generating sufficient piezopotential, and ensuring a high amount of active sites [20]. Recent advancements are focusing on integrating piezocatalysis with electro- and photocatalysis using hybrid materials with a build in Schottky junction [21–23]. Further enhancements in piezopotential are being explored through doping, and the engineering of morphology and defects [24–27].

Among various piezocatalyst materials, ZnO stands out for its environmental friendliness and biocompatible [28]. In this work, we have synthesized two distinct ZnO microstructures: flower-like ZnO (F-ZnO) and rod-like ZnO (R-ZnO). The piezoelectric properties of these two materials, although the materials themselves have been utilized in other contexts, have never before been investigated or exploited in the field of piezocatalysis [29,30]. We explored how two key factors, (1) structural deformability, and (2) the intensity of the applied stress, affect their piezocatalytic performance. Given the same intensity of applied stress, it is evident that an anisotropic structure like R-ZnO, with its elongated shape, is inherently more deformable compared to a more spherical or compact structure like F-ZnO. This inherent flexibility should maximize the formation of the piezopotential in anisotropic structures. To further evaluate the impact of the applied stress, we evaluated the mechanical response of these materials under various ultrasound frequencies. This allowed us to assess how different stress intensities influence behaviour of both materials. Both structures were confirmed to possess piezoelectric properties and were evaluated for their efficacy in degrading methylene blue (MB) through ultrasound-stimulated piezocatalysis, particularly focusing on water oxidation reactions (Eqs. 3, 4, and 7) leading to hydroxyl radicals and superoxide anions formation. Our experiments reveal that the optimal activity occurred at an ultrasound frequency of 35 kHz. Notably, R-ZnO, with its anisotropic structure, showed significant piezocatalytic efficiency under these conditions.

Interestingly, dye degradation was even achieved in the absence of atmospheric oxygen, suggesting that ZnO was able to produce O_2 directly from water. These findings underscore the unique capabilities of R-ZnO marking a significant advancement in piezocatalysis without reliance on hybrid materials or the combination with additional catalytic processes [31,32]. This work sets a foundation for further exploration of ZnO-based piezocatalysts in environmental and energy applications such as nitrogen fixation and methane conversion.

2. Materials and methods

2.1. Synthesis of ZnO microstructures

Flower-like shaped ZnO microstructures (F-ZnO) were synthetized according to a slightly modified chemical precipitation procedure [29]. In a typical experiment, 35 mL of NaOH (4 M) solution were added dropwise to 50 mL zinc sulphate heptahydrate (99.95 %, Merck) 1 M aqueous solution. The mixture was kept under vigorous stirring at 4°C for 30 min. Then, MilliQ grade water was added to the precursor mixture to reach the final volume of 100 mL. The precursor was so heated for 2 h at 90°C. The white precipitate was washed three times with MilliQ grade water through static precipitation and finally dried in air at 100°C for 2 h in a static oven. The white powder was then stored in the dark at room temperature (R.T.) or used as such for further experiments.

Rod-like shaped ZnO microstructures (R-ZnO) were also prepared by means of a chemical precipitation procedure [30] by using zinc nitrate hexahydrate (99 %, Merck) as precursor and ammonia hydroxide (25 %, Merck) to reach pH 10 in the reaction mixture, which was then kept at 95°C for 7 h under stirring on a hot plate. The white R-ZnO precipitate was separated by gravity, washed (3 times) with MilliQ grade water and after it was dried in air for 14 h at 100 °C in a static oven. The white powder was then stored in the dark at R.T. or used as such for further experiments.

2.2. Morphological and physical-chemical characterisation

The synthesized materials were characterised using Raman spectroscopy. The compounds, in powder form, were illuminated with a 532 nm laser at a power of 0.125 $mWcm^{-2}$. Each spectrum was acquired with 30 scans in the 180–900 cm^{-1} range of using a Horiba Xplora microRaman.

The powder X-ray diffraction patterns were recorded with a Malvern Panalytical Empyrean diffractometer in transmission geometry, equipped with a PIXcel3D solid-state detector and a Cu anode X-ray source (Cu Kα1: 1.5406 Å; Cu Kα2: 1.5444 Å). The powder X-ray diffraction patterns were recorded between 15 and 70 2theta degrees at a scan rate of 0.013 ∘ /s.

Scanning Electron Microscopy (SEM) investigations were performed on a FEI-Q FEG250 instrument.

Specific surface area and pore size distribution of the ZnO rods and flowers were measured by Brunauer-Emmett-Teller (BET) method from the N_2 adsorption-desorption isotherm curve using a Anton Parr NOVA 2200e surface area analyzer. Prior to BET surface area measurements, respective powder samples were degassed at 100°C for 12 h under vacuum and the adsorption-desorption isotherm was performed at −196°C using N_2 as the adsorbent gas.

2.3. Piezo force microscopy measurements and Finite Element Method (FEM) simulations

A film of F-ZnO and R-ZnO was deposited through immersion and emersion of an indium tin oxide (ITO) substrate in a 2-propanol (ACS reagent, ≥99.5 %, Merck) suspension of the two zinc oxide structures. Piezo Force Microscopy (PFM) measurements [33] were conducted using a SmartSPM 1000 AIST-NT HORIBA with an applied potential in the range of −5 V to 5 V, with an acquisition step of 0.1 V. Finite Element Method (FEM) simulations were implemented using Comsol Multiphysics software, considering the dimensions obtained through electron scanning microscopy for modelling [34].

2.4. Piezocatalytic methylene blue degradation and piezoproduced O_2 quantification experiments

The piezocatalytic experiments have been conducted using sonicator

cleaning machines (Misumi GmbH) for the frequencies operating at 35, 42 and 50 KHz (power 100 W) to induce the mechanical stress. The ultrasound stimulus at 60 KHz was obtained using an ultrasound bath from purchased from Thermo Fisher Scientific (power 140 W).

Methylene blue (MB) was used as a standard molecule to monitor the piezocatalytic degradation efficiency of F-ZnO and R-ZnO. In a typical experiment, 0.2 g/L of piezocatalyst were suspended in a MB aqueous solution (5×10^{-5} M) and ultrasounds were applied for 60 min in dark. All the measurements have been performed in isothermal conditions (25 $\pm$ 0.5 °C) by maintaining the temperature by means of an external flux of water at controlled temperature to avoid the thermal influence on the reaction kinetics. The degradation monitored as the reduction of the MB absorption at 670 nm [35] was recorded with a Perkin Elmer Lambda 650 UV-Vis spectrophotometer.

The degradation efficiency (%) was calculated as $(C_0\text{-}C)/C_0$ x 100, where A_0 refers to MB initial absorbance and A refers to the absorbance recorded at each time point, which is correlated to MB concentration according to the Lambert-Beer law [36].

MB degradation mechanism was investigated by means of reactive species scavenging tests, specifically, 2-propanol (ACS reagent, $\geq$99.5 %, Merck) and L-ascorbic acid (Merck) were used to scavenge hydroxyl radicals and superoxide ions, respectively. The piezodegradation experiments with 1 mM of these scavengers were carried out as reported above. Ascorbic acid was also tested at increasing concentration (1, 10 and 25 mM) in other experiments.

The production of oxygen following sonication was monitored and quantified as concentration of dissolved oxygen. The experimental layout consisted of a container in which the piezocatalyst was dispersed (0.2 g/L), and the O_2 sensor (DO500 benchtop meter, Clean Instrument) was submerged. The entire system was bubbled with argon for 10 minutes, sealed and placed in the ultrasonic bath, and the ultrasounds stimulus (35 kHz) was applied. Dissolved oxygen was measured using the benchtop meter operating in the 0.0–400.0 % saturation percentage range with a resolution of 0.1 %, which corresponds to a range of 0.00–40.00 mg/L (resolution of 0.01 mg/L).

3. Results and discussion

3.1. Morphological and structural materials' characterisation

F-ZnO and R-ZnO were synthetized as described in the Experimental section and characterized by powder X-ray diffraction (PXRD). Both materials exhibited the piezoresponsive zincite crystal structure [37] (see supplementary material). The characteristic peaks for the R- and F-ZnO structures were found at 31.77, 31.79 (100), 34.41, 34.43 (002), 36.25, 36.27 (101), 47.55, 47.57 (102), 56.60, 56.63 (110), 62.85, 62.90 (103), 66.37, 66.41 (200), 67.94, 67.93 (112) 69.08, 69.14 (201) and indexed according to the JCPDS card # 80–007. Raman spectroscopy (see supplementary material) further confirmed the wurtzite crystalline form [38,39], with the predominant peak at 435 cm^{-1}, corresponding to the E_2 vibration [40,41]. Additionally, signals for the A_1-TO vibration at 380 cm^{-1}; and the $2E_2$ mode at 330 cm^{-1} [42,43] were observed, indicating the structural integrity and similarity of both nanostructures [44,45].

Scanning electron microscopy revealed significant differences in morphology between the two ZnO materials with rod-like and flower-like forms (see supplementary material) [30,46]. Porosity assessment via N_2 adsorption isotherm showed that F-ZnO has a higher specific surface area and pore volume compared to R-ZnO (see supplementary material).

3.2. Piezo Force Microscopy (PFM) and piezoelectric analysis of ZnO materials

PFM was used to evaluate the piezoelectric behaviour of both ZnO materials. Generally, the strain induced in a piezoelectric material is directly proportional to the intensity of the applied electric field, causing expansion or contraction based on the direction and sense of the electric field vector. We assessed the ZnO properties by recording the strain and polarization responses to the applied electric field, testing the hypothesis that anisotropic structures like R-ZnO would exhibit larger piezoelectric responses [47]. For both materials (Fig. 1) the typical hysteretic curves were obtained with notable amplitude variations upon external electric field application (black lines) [48]. The phase hysteresis loops in the PFM phase, indicative of the Weiss domains orientation [49], confirmed the piezoelectric properties of both F-ZnO and R-ZnO. The phase angle variation of about 100° in the F-ZnO material and up to 150° in R-ZnO suggest that R-ZnO may have a more orientable domain structure, allowing for greater range of polarization orientation under applied fields. The total displacement measured for F-ZnO was about 1.75 nm, while for R-ZnO it reached 3 nm under similar electric field conditions, indicating a stronger piezoelectric effect in R-ZnO. This can be attributed to its anisotropic structure, which likely enhances its piezoelectric response due to more effective alignment of piezoelectric domains or better mechanical flexibility that allows for greater deformation under electric stress. These findings support our initial hypothesis that structural deformability, influenced by anisotropy, significantly affects piezoelectric responses. Moreover, the intensity of the applied stress, consistent across both materials, highlights how intrinsic material properties like structural anisotropy dictate the piezoelectric performance, aligning with our exploration of key factors affecting their piezocatalytic performance.

Finite element method (FEM) simulations were conducted to analyse the piezopotential generation under simulated mechanical stress, assuming cavitation bubble implosion at 35 kHz produces a pressure of 10^8 Pa [50]. The simulations revealed that R-ZnO undergo higher mechanical stress due to their elongated, nearly one-dimensional, geometry, which is more easily deformable compared to the two-dimensional F-ZnO structure (Figs. 1d and 1b). This mechanical deformation in piezoelectric materials results in the generation of a piezopotential, with R-ZnO exhibiting an induced piezopotential nearly an order of magnitude larger than F-ZnO structures (approximately 10 V vs. 1 V far from the boundary of the structures, Figs. 1e and 1c).

3.3. Piezoelectric production of radicals and MB degradation

The PFM and FEM results, which confirm electrical polarization in the structures following mechanical deformation, led us to explore the piezoelectric properties, of both materials in the piezo-assisted degradation of methylene blue (MB). For this, 0.2 g/L ZnO was dispersed in a 5×10^{-5} M aqueous MB solution and subjected to mechanical stress in an ultrasonic bath, taking advantage of the energy released from the implosion of the cavitation bubble; the sound waves in the ultrasonic range promote cavitation bubble formation, which upon imploding induce local deformation in the nanostructures [50].

Fig. 2a illustrates the MB degradation efficiency (DE%) over time, showing that R-ZnO achieved over 95 % degradation efficiency in just 30 minutes under ultrasound at 35 kHz. The superior performance of R-ZnO is primarily due to its more efficient generation of piezopotential in its elongated structure, as opposed to the more compact F-ZnO. Despite F-ZnO's higher porosity (see supplementary material), which typically aids in cavitation bubble nucleation and analyte molecules adsorption [51–53], R-ZnO consistently demonstrated higher degradation rates. This suggest that the efficiency of MB piezodegradation is more strongly influenced by the generation of piezopotential.

According to the screening effect theory [15], the piezoelectric degradation of aqueous dissolved compounds is primarily driven by the formation of radical species. Fig. 2b illustrates this process schematically.

Initially, the piezoelectric system, when not subjected to any mechanical stress, remains in a neutral state (Fig. 2b scheme i). Upon applying mechanical stress, the polarization of the piezoelectric material

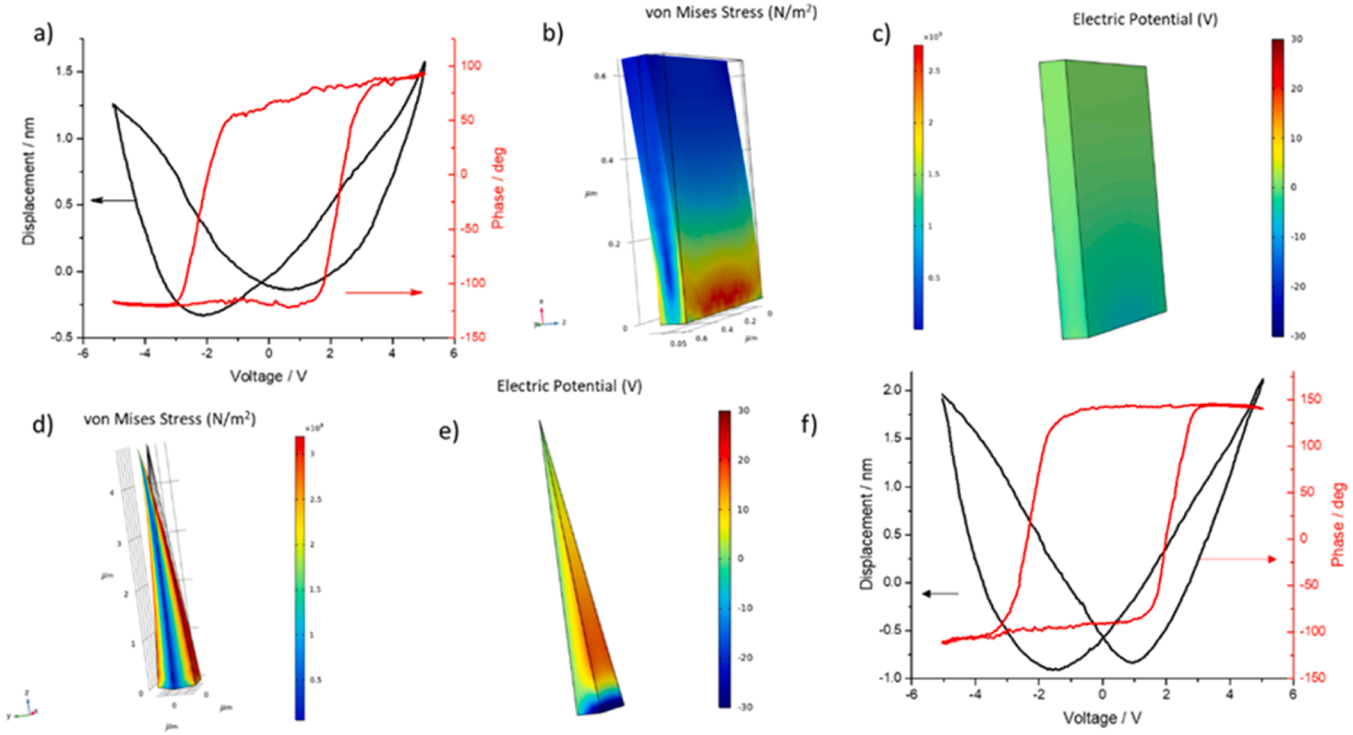

Fig. 1. Evaluation and simulation of piezoelectric properties of ZnO materials. a,f) Displacement and phase variation induced by an AFM tip graphed respectively in black and red for F-ZnO (a) and for R-ZnO (f). b,c) F-ZnO modeled using FEM. (b) Deformation and mechanical stress, (c) Distribution of piezogenerated electric potential, both resulting from the implosion of a cavitation bubble at 10^8 Pa. d,e) Similar simulations for R-ZnO. All ZnO materials were modeled using morphological data obtained from SEM microscopy.

increases, meaning the dipole moment generated by the displacement charges within the material intensifies. To ensure local charge neutrality, screening charges (SC) will be generated: on the face of R-ZnO where positive charges accumulate, an equivalent number of negative charges (SC^-) will be attracted from the aqueous environment, promoting an oxidation reaction of water (Fig. 2b scheme ii). Conversely, on the opposite side of the semiconductor, positive charges (SC^+) from the environment will be required, promoting a reduction reaction. When the external mechanical stimulus ceases, the internal neutrality of R-ZnO is restored, and the screening charges accumulated on both faces of the piezoelectric material will be released into the aqueous environment (Fig. 2b scheme iii). The positive charges previously accumulated on the negatively charged face of R-ZnO will catalyse oxidation reactions, while the negative screening charges will catalyse reduction reactions in the surrounding medium [32]. When the piezoelectric material is subjected to opposite stress, that is tension (Fig. 2b scheme iv), an effect identical to that described in Fig. 2b scheme ii, but on the opposite faces of the ZnO, will be observed. The typical reactions occurring during these processes can be summarized as following oxidation:

$2H_2O \rightarrow O_2 + 4H^+ + 4SC^-$ (Fig. 2bscheme ii – ox)

$H_2O \rightarrow \cdot OH + H^+ + SC^-$ (Fig. 2bscheme ii – ox)

$2H_2O + 4SC^+ \rightarrow O_2 + 4H^+$ (Fig. 2b scheme iii – ox)

$H_2O + SC^+ \rightarrow \cdot OH + H^+$ (Fig. 2b scheme iii – ox)

and reduction reactions:

$O_2 \rightarrow \cdot O_2^- + SC^+$ (Fig. 2b scheme ii – red)

$4H^+ \rightarrow 2H_2 + 4SC^+$ (Fig. 2bscheme ii – red)

$O_2 + SC^- \rightarrow \cdot O_2^-$ (Fig. 2bscheme iii – red)

$4H^+ + 4SC^- \rightarrow 2H_2$ (Fig. 2b scheme iii – red)

These reactions highlight how piezoelectrically generated electric fields promote both oxidation and reduction processes in water, leading to the formation of reactive oxygen species such as superoxide and hydroxyl radicals. These radicals play a crucial role in the degradation of organic pollutants, effectively enhancing water purification technologies.

The piezodegradation process of MB was monitored in presence of 2-propanol and ascorbic acid as scavengers of hydroxyl radicals and superoxide ions, respectively. The role of both scavengers, after 60 minutes of ultrasound treatment, appears negligible when R-ZnO is used (Fig. 2c). On the contrary, the piezocatalytic properties of F-ZnO structures towards MB are influenced by both the hydroxyl radical scavenger and the superoxide ion scavenger. However, it must be considered that ascorbic acid strongly inhibits the degradation efficiency of MB, suggesting that the catalytic process is primarily mediated by the action of superoxide ions [54,55]. In the case of R-ZnO, it can be hypothesized that the piezopotential generated on the surface of the elongated structures, as a result of cavitation bubble implosion induced by ultrasound stimulation, is so intense that it efficiently promotes the formation of large amounts of radicals. In support of this rationalization, the degradation efficiency was monitored in the presence of increasing concentrations of ascorbic acid (see supplementary material). By increasing the concentration of ascorbic acid in the MB piezodegradation experiments the degradation efficiency results significantly influenced, reducing from 95 % in the absence of superoxide ion scavenger to approximately 30 % in the presence of ascorbic acid at a concentration of 25 mM. This confirms the proposed hypothesis that the high piezopotential generated on R-ZnO is capable of producing a much larger quantity of superoxide ions compared to F-ZnO. In this condition,

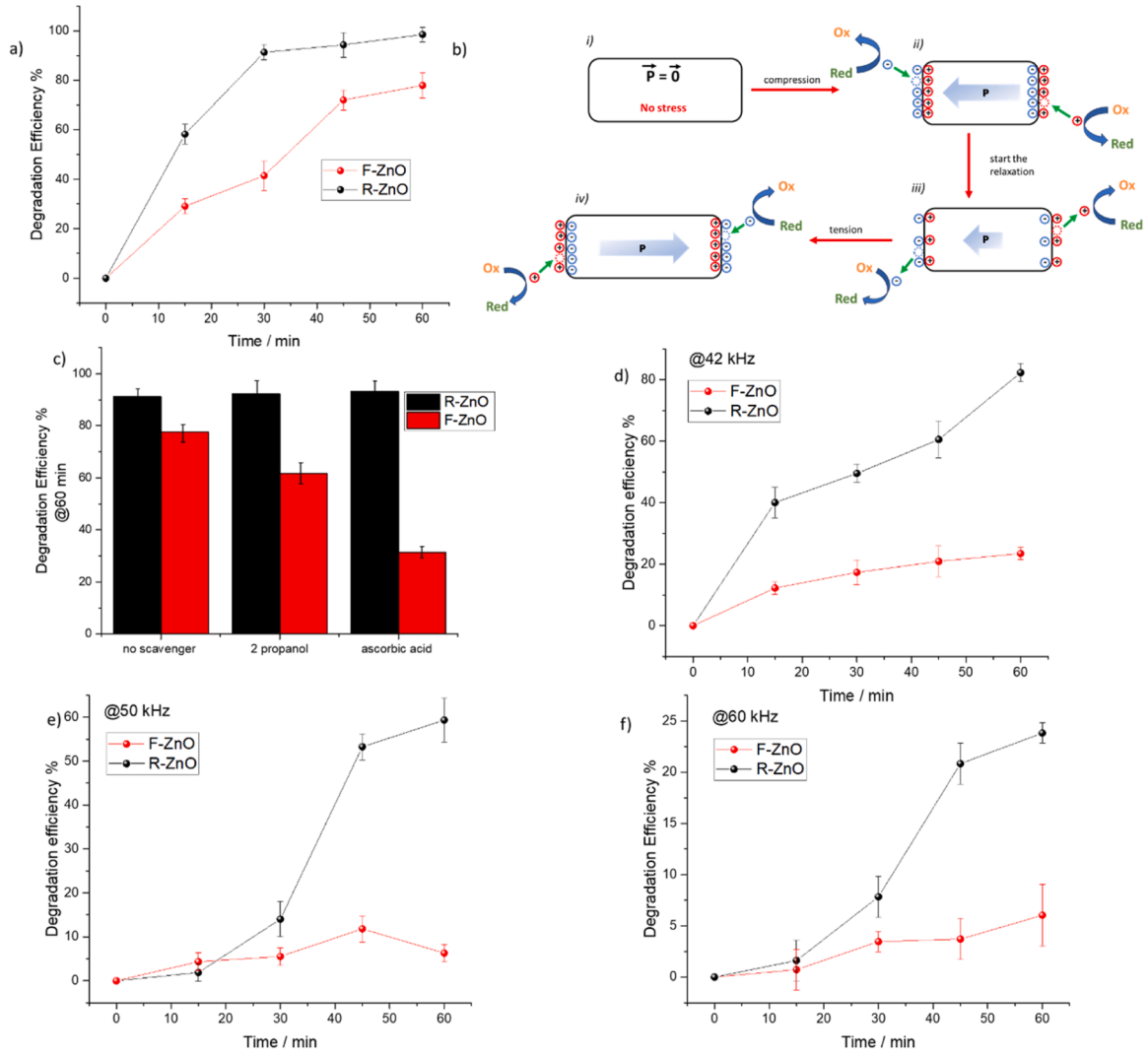

Fig. 2. a) Degradation efficiency of methylene blue degradation following ultrasound stimuli (at 35 kHz) in the presence of zinc oxide-based structures. b) Schematic representation of radicals' formation as a consequence of the piezopotential induced by an alternate mechanical stress on a piezoelectric material. c) Influence of superoxide ion scavenger (ascorbic acid) and hydroxyl radical scavenger (2-propanol) on the degradation efficiency of MB at 35 kHz ultrasound. d) The influence of the frequency used to stimulate the piezopotential on the degradation efficiency of MB (R-ZnO structures plotted in black and F-ZnO structures graphed in red) was evaluated performing the experiments setting the ultrasound bath frequency at 35, 42, 50 and 60 kHz. Each measurement was repeated three times and the average value was reported.

a higher concentration of O_2^- scavenger is necessary to inhibit the MB piezodegradation process.

Cavitation bubbles generated by ultrasonic stimulation primarily cause micro-jets and shock waves, [56] leading to localized pressure increase. The velocity of these micro-jets depends on the radius of the imploding cavitation bubble, which in turn affects the energy released during the bubble's collapse. Consequently, the frequency of the applied ultrasound influences the amount of energy released and the resulting pressure exerted on the ZnO material. To assess this effect, we varied the ultrasonic frequencies while maintaining constant power.

MB degradation experiments were conducted at 35 kHz, 42 kHz, 50 kHz, and 60 kHz with released energy decreasing as frequency increases (Fig. 2d) [50]. Higher frequencies resulted in lower piezopotential and reduced degradation efficiency for both R-ZnO and F-ZnO (see supplementary material). Specifically, R-ZnO achieved degradation efficiencies of approximately 95 %, 82 %, 60 %, and 24 % at these frequencies. F-ZnO showed a similar trend with efficiencies decreasing from 78 % at 35 kHz to 23 %, 11 %, and 6 % at higher frequencies.

As observed in the previous reported experiments conducted at 35 kHz, even at 42 kHz, the presence of scavengers at 1 mM concentration negligibly influences the piezodegradation efficiency of MB by R-ZnO (see supplementary material). With the increase in ultrasound frequencies, i.e., the decrease in induced piezopotentials, R-ZnO structures also become significantly affected by the presence of ascorbic acid and, to a lesser extent, by 2-propanol (see supplementary material). The lower magnitude of the piezopotential produced on F-ZnO, on the other hand, causes scavengers to almost completely inhibit the piezodegradation at both 50 and 60 kHz, and to significantly reduce at 42 kHz.

3.4. *Piezoelectrically induced O_2 evolution*

The outstanding MB degradation performances prompted us to investigate the piezocatalytic oxygen evolution reaction [57]. We measured the oxygen production under various conditions: with and without ZnO nanostructures, and with and without the application of ultrasound stimulation (Fig. 3a).

The O_2 production from water under ultrasound stimulation with F-ZnO stabilizes rapidly at approximately 300 μmol g^{-1} (red squares). As expected, without ultrasound stimulus (blue diamonds) no O_2

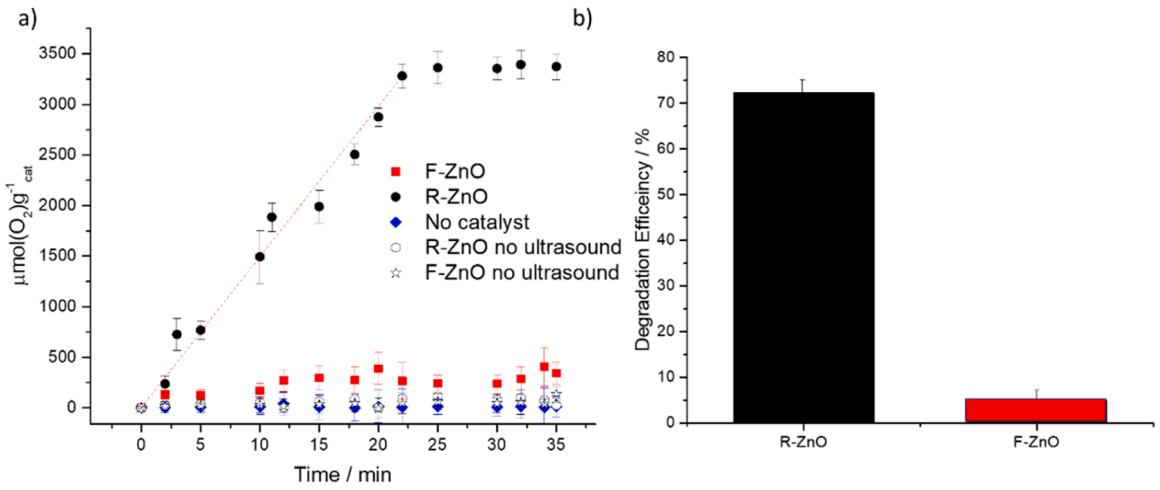

Fig. 3. a) Kinetics of piezo-induced production of O_2 in a hermetically sealed container in the presence of R-ZnO (black dots), in the presence of F-ZnO (red squares), and in the absence of a catalyst (blue diamonds) and external stimuli (white circles and stars). b) Degradation efficiency of MB monitored in the absence of atmospheric oxygen.

generation was observed. Interestingly, R-ZnO (black dots), is much more efficient in the OER with continuously increasing concentrations that exceed the detection range of our detector translating into 10 mmol $O_2 \cdot g^{-1}$ (ZnO) h^{-1} in just 20 minutes. This suggests that the piezopotential induced by cavitation bubble implosion in R-ZnO suspension is sufficient to drive O_2 evolution via water splitting (Eq. 2) [57]. This finding is very promising since most reported oxygen evolution systems involve the combination of piezocatalysis with co-catalyst, doping atoms, electrochemistry [58–61]. Further, the possibility to re-use R-ZnO in the OER was monitored. After the first cycle (upon 20 min ultrasounds stimulation), the catalyst was recovered by centrifugation and re-suspended in fresh medium for other three times (see supplementary material). The performance, very interestingly, showed minimal variation, indicating the recyclability of the system.

This observation led us to study the degradation of MB in anaerobic conditions within a hermetically sealed vial containing 10 mL aqueous MB (5×10^{-5} M) solution with 0.2 g/L ZnO and purged with argon before sealing. While only limited MB degradation was observed after 30 minutes (35 kHz) with F-ZnO, R-ZnO lead to a marked decrease (DE 70 %) (Fig. 3b and see supplementary material). This further confirms the potential of R-ZnO to produce significant amounts of oxygen from water.

4. Conclusions

This study synthesized two distinct ZnO morphologies: elongated R-ZnO, and more compact F-ZnO, both demonstrating piezoelectric characteristics as seen with piezoforce microscopy. Our investigations focused on how structural deformability and the intensity of applied stress influence piezocatalytic performance. We found that R-ZnO, with its elongated structure, was not only more efficient in MB degrading, achieving over 90 % degradation of the 5×10^{-5} M solution (10 mL) after 60 minutes (35 kHz) with 2 mg, but also remarkable in catalysing oxygen evolution from water at over 10 mmol O_2 g^{-1} h^{-1}. In contrast, the bidimensional F-ZnO, despite achieving a 78 % degradation efficiency, showed a lesser capability for oxygen evolution.

Moreover, the effect of the ultrasonic frequency on the piezocatalytic activity was substantial, with optimal performance observed for the lowest frequency (35 kHz) used. This finding suggests the need for further studies to explore the impact of lower frequencies, below 35 kHz, to fully understand the frequency-dependent behaviour of piezopotential generation and its influence on catalytic performance.

These findings underscore the importance of nanostructure morphology in enhancing piezocatalytic activity and open avenues for further research into optimizing these structures for environmental remediation and sustainable chemical processes. Understanding and manipulating structural deformability and stress intensity will be crucial in maximizing the efficacy of piezoelectric materials in practical applications.

Author contributions

The manuscript was written through contributions of all authors. All authors have given approval to the final version of the manuscript.

CRediT authorship contribution statement

Sudipto Pal: Investigation. **Johan Hofkens:** Writing – review & editing, Conceptualization. **Donato Valli:** Methodology, Investigation. **Michela Ottolini:** Investigation. **Rosanna Pagano:** Writing – original draft, Investigation. **Simona Bettini:** Writing – original draft, Methodology, Investigation, Conceptualization. **Ludovico Valli:** Supervision, Funding acquisition, Conceptualization. **Maarten Roeffaers:** Writing – review & editing, Conceptualization. **Gabriele Giancane:** Writing – review & editing, Supervision, Methodology, Conceptualization.

Declaration of Competing Interest

The authors declare that they have no known competing financial interests or personal relationships that could have appeared to influence the work reported in this paper.

Data Availability

Data will be made available on request.

Acknowledgements

This research was supported by the PRIN 2022 (protocol number 20228YFRNL), by the PRIN PNRR 2022 (protocol number P2022WLAY7) and by the Research Foundation – Flanders through an FWO doctoral fellowship (FWO Grant Number 1S45223N).

Appendix A. Supporting information

Supplementary data associated with this article can be found in the online version at doi:10.1016/j.jece.2024.114312.

References

[1] R. Xu, H. Huang, W. Wang, L. Ding, Q. Lin, J. Li, Y. Zhang, Y. Han, J. Wang, X. Lu, Direct conversion of water to hydrogen peroxide on single electrode towards partial oxidation of propylene, Chem. Eng. J. 461 (2023) 141748, https://doi.org/10.1016/j.cej.2023.141748.

[2] T.-Y. Shuai, Q.-N. Zhan, H.-M. Xu, Z.-J. Zhang, G.-R. Li, Recent developments of MXene-based catalysts for hydrogen production by water splitting, Green. Chem. 25 (2023) 1749–1789, https://doi.org/10.1039/D2GC04205C.

[3] T. Hisatomi, K. Domen, Reaction systems for solar hydrogen production via water splitting with particulate semiconductor photocatalysts, Nat. Catal. 2 (2019) 387–399, https://doi.org/10.1038/s41929-019-0242-6.

[4] P. Hota, A. Das, D.K. Maiti, A short review on generation of green fuel hydrogen through water splitting, Int. J. Hydrog. Energy 48 (2023) 523–541, https://doi.org/10.1016/j.ijhydene.2022.09.264.

[5] M. El ouardi, A. El Idrissi, M. Arab, M. Zbair, H. Haspel, M. Saadi, H. Ait Ahsaine, Review of photoelectrochemical water splitting: From quantitative approaches to effect of sacrificial agents, oxygen vacancies, thermal and magnetic field on (photo) electrolysis, Int. J. Hydrog. Energy 51 (2024) 1044–1067, https://doi.org/10.1016/j.ijhydene.2023.09.111.

[6] B. Rani, A.K. Nayak, N.K. Sahu, 1 - Fundamentals principle of photocatalysis, in: A. K. Nayak, N.K. Sahu (Eds.), Nanostructured Materials for Visible Light Photocatalysis, Elsevier, 2022, pp. 1–22, https://doi.org/10.1016/B978-0-12-823018-3.00009-9.

[7] F.M. Sapountzi, J.M. Gracia, C.J. (Kees-J. Weststrate, H.O.A. Fredriksson, J.W. (Hans) Niemantsverdriet, Electrocatalysts for the generation of hydrogen, oxygen and synthesis gas, Prog. Energy Combust. Sci. 58 (2017) 1–35, https://doi.org/10.1016/j.pecs.2016.09.001.

[8] M. Kumar, B. Meena, P. Subramanyam, D. Suryakala, C. Subrahmanyam, Recent trends in photoelectrochemical water splitting: the role of cocatalysts, NPG Asia Mater. 14 (2022) 1–21, https://doi.org/10.1038/s41427-022-00436-x.

[9] S. Liu, H. Zhang, Y. Wang, H. Sun, S. Wang, W. Tian, Morphology-enhanced piezoelectric performance of SnS nanobelts for acetaminophen degradation, J. Mater. Chem. A (2024), https://doi.org/10.1039/D4TA02531H.

[10] K. Wang, C. Han, J. Li, J. Qiu, J. Sunarso, S. Liu, The Mechanism of piezocatalysis: energy band theory or screening charge effect? Angew. Chem. Int. Ed. 61 (2022) e202110429 https://doi.org/10.1002/anie.202110429.

[11] S. Lan, C. Yu, F. Sun, Y. Chen, D. Chen, W. Mai, M. Zhu, Tuning piezoelectric driven photocatalysis by La-doped magnetic BiFeO3-based multiferroics for water purification, Nano Energy 93 (2022) 106792, https://doi.org/10.1016/j.nanoen.2021.106792.

[12] S. Tu, Y. Guo, Y. Zhang, C. Hu, T. Zhang, T. Ma, H. Huang, Piezocatalysis and Piezo-Photocatalysis: Catalysts Classification and Modification Strategy, Reaction Mechanism, and Practical Application, Adv. Funct. Mater. 30 (2020) 2005158, https://doi.org/10.1002/adfm.202005158.

[13] R. Su, H.A. Hsain, M. Wu, D. Zhang, X. Hu, Z. Wang, X. Wang, F. Li, X. Chen, L. Zhu, Y. Yang, Y. Yang, X. Lou, S.J. Pennycook, Nano-ferroelectric for high efficiency overall water splitting under ultrasonic vibration, Angew. Chem. Int. Ed. 58 (2019) 15076–15081, https://doi.org/10.1002/anie.201907695.

[14] W. Zheng, Y. Tang, C. Jia, Z. Liu, Z. Zhang, K. Zhao, Resonance of KNbO3 nanofibers is effectively stimulated by ultrasound with low frequency and low power to enhance piezocatalytic activity, J. Mater. Chem. A 12 (2024) 11378–11389, https://doi.org/10.1039/D3TA08028E.

[15] N. Meng, W. Liu, R. Jiang, Y. Zhang, S. Dunn, J. Wu, H. Yan, Fundamentals, advances and perspectives of piezocatalysis: a marriage of solid-state physics and catalytic chemistry, Prog. Mater. Sci. 138 (2023) 101161, https://doi.org/10.1016/j.pmatsci.2023.101161.

[16] S. Qu, H. Wu, Y.H. Ng, Solar Oxidative Hydrogen Peroxide Production: Is the Oxygen Vacancy Always a Promoter in Solar Water Oxidation? ACS Catal. 14 (2024) 5297–5304, https://doi.org/10.1021/acscatal.3c05764.

[17] M. Dan, R. Zhong, S. Hu, H. Wu, Y. Zhou, Z.-Q. Liu, Strategies and challenges on selective electrochemical hydrogen peroxide production: Catalyst and reaction medium design, Chem. Catal. 2 (2022) 1919–1960, https://doi.org/10.1016/j.checat.2022.06.002.

[18] C. Dong, W. Fang, Q. Yi, J. Zhang, A comprehensive review on reactive oxygen species (ROS) in advanced oxidation processes (AOPs), Chemosphere 308 (2022) 136205, https://doi.org/10.1016/j.chemosphere.2022.136205.

[19] C. Su, C. Li, R. Li, W. Wang, Insights into highly efficient piezocatalytic molecule oxygen activation over Bi2Fe4O9: Active sites and mechanism, Chem. Eng. J. 452 (2023) 139300, https://doi.org/10.1016/j.cej.2022.139300.

[20] S. Zhao, M. Liu, Y. Zhang, Z. Zhao, Q. Zhang, Z. Mu, Y. Long, Y. Jiang, Y. Liu, J. Zhang, S. Li, X. Zhang, Z. Zhang, Harvesting mechanical energy for hydrogen generation by piezoelectric metal–organic frameworks, Mater. Horiz. 9 (2022) 1978–1983, https://doi.org/10.1039/D1MH01973B.

[21] L. Pan, S. Sun, Y. Chen, P. Wang, J. Wang, X. Zhang, J.-J. Zou, Z.L. Wang, Advances in piezo-phototronic effect enhanced photocatalysis and photoelectrocatalysis, Adv. Energy Mater. 10 (2020) 2000214, https://doi.org/10.1002/aenm.202000214.

[22] G. Jiang, L. Xie, W. Huang, Y. Liu, X. Lu, Y. Xin, Z. Zhou, X. Fan, The influence of lowing the Schottky barrier on the reactive oxygen species formation in Ag@SrBi2Ta2O9 piezocatalyst under ball milling, Chem. Eng. J. 491 (2024) 152085, https://doi.org/10.1016/j.cej.2024.152085.

[23] S. Zhong, G. Liu, B. Liu, W. Wang, Q. Zhang, X. Ru, L. Zhang, Piezoelectric shield Schottky barrier coupling LSPR effect promoted the elimination of 2,4-dichlorophenol by Bi@Bi2WO6, Appl. Surf. Sci. 648 (2024) 158939, https://doi.org/10.1016/j.apsusc.2023.158939.

[24] X. Xiong, Y. Wang, J. Ma, Y. He, J. Huang, Y. Feng, C. Ban, L.-Y. Gan, X. Zhou, Oxygen vacancy engineering of zinc oxide for boosting piezo-electrocatalytic hydrogen evolution, Appl. Surf. Sci. 616 (2023) 156556, https://doi.org/10.1016/j.apsusc.2023.156556.

[25] B. Yuan, J. Wu, N. Qin, E. Lin, Z. Kang, D. Bao, Sm-doped Pb(Mg1/3Nb2/3)O3-xPbTiO3 piezocatalyst: Exploring the relationship between piezoelectric property and piezocatalytic activity, Appl. Mater. Today 17 (2019) 183–192, https://doi.org/10.1016/j.apmt.2019.07.015.

[26] E. Lin, J. Wu, N. Qin, B. Yuan, Z. Kang, D. Bao, Enhanced piezocatalytic, photocatalytic and piezo-/photocatalytic performance of diphasic $Ba_{1-x}Ca_xTiO_3$ nanowires near a solubility limit, Catal. Sci. Technol. 9 (2019) 6863–6874, https://doi.org/10.1039/C9CY01713E.

[27] M. Sharma, G. Singh, R. Vaish, Dye degradation and bacterial disinfection using multicatalytic $BaZr_{0.02}Ti_{0.98}O_3$ ceramics, J. Am. Ceram. Soc. 103 (2020) 4774–4784, https://doi.org/10.1111/jace.17171.

[28] O. Oleshko, Y. Husak, V. Korniienko, R. Pshenychnyi, Y. Varava, O. Kalinkevich, M. Pisarek, K. Grundsteins, O. Pogorielova, O. Mishchenko, W. Simka, R. Viter, M. Pogorielov, Biocompatibility and Antibacterial Properties of ZnO-Incorporated Anodic Oxide Coatings on TiZrNb Alloy, Nanomater. (Basel) 10 (2020) 2401, https://doi.org/10.3390/nano10122401.

[29] A. Taufiq, H.N. Ulya, C.I. Yogihati, Sunaryono, N. Hidayat, N. Mufti, Masruroh, S. Soda, T. Ishida, Effects of ZnO nanoparticles on the antifungal performance of Fe3O4/ZnO nanocomposites prepared from natural sand, Adv. Nat. Sci: Nanosci. Nanotechnol. 11 (2020) 045004, https://doi.org/10.1088/2043-6254/abb8c6.

[30] A. Fioravanti, P. Marani, S. Morandi, S. Lettieri, M. Mazzocchi, M. Sacerdoti, M. C. Carotta, Growth mechanisms of Zno micro-nanomorphologies and their role in enhancing gas sensing properties, Sensors 21 (2021) 1331, https://doi.org/10.3390/s21041331.

[31] R.K. Pandey, J. Dutta, S. Brahma, B. Rao, C.-P. Liu, Review on ZnO-based piezotronics and piezoelectric nanogenerators: aspects of piezopotential and screening effect, J. Phys. Mater. 4 (2021) 044011, https://doi.org/10.1088/2515-7639/ac130a.

[32] Y.-L. Hsiao, P.-C. Chen, K. Gupta, C.-C. Lai, Y.-C. Pu, C.-P. Liu, Piezocatalytic and doping effects synergistically enhance the oxygen evolution in Sb-doped zinc oxide nanorod arrays as a photoanode for photoelectrochemical water splitting, MRS Energy Sustain. 9 (2022) 19–27, https://doi.org/10.1557/s43581-022-00021-3.

[33] M.-H. Zhao, Z.-L. Wang, S.X. Mao, Piezoelectric Characterization of individual zinc oxide nanobelt probed by piezoresponse force microscope, Nano Lett. 4 (2004) 587–590, https://doi.org/10.1021/nl035198a.

[34] V.-T. Nguyen, P. Kumar, J. Leong, Finite Element Modellingand Simulations of Piezoelectric Actuators Responses with Uncertainty Quantification, Computation 6 (2018) 60, https://doi.org/10.3390/computation6040060.

[35] D. Zhang, F. Dai, P. Zhang, Z. An, Y. Zhao, L. Chen, The photodegradation of methylene blue in water with PVDF/GO/ZnO composite membrane, Mater. Sci. Eng.: C. 96 (2019) 684–692, https://doi.org/10.1016/j.msec.2018.11.049.

[36] S. Bettini, R. Pagano, D. Valli, C. Ingrosso, M. Roeffaers, J. Hofkens, G. Giancane, L. Valli, ZnO nanostructures based piezo-photocatalytic degradation enhancement of steroid hormones, Surf. Interfaces 36 (2023) 102581, https://doi.org/10.1016/j.surfin.2022.102581.

[37] F.R. Fan, W. Tang, Z.L. Wang, Flexible Nanogenerators for Energy Harvesting and Self-Powered Electronics, Adv. Mater. 28 (2016) 4283–4305, https://doi.org/10.1002/adma.201504299.

[38] A. Khorsand Zak, W.H. Abd. Majid, M.E. Abrishami, R. Yousefi, X-ray analysis of ZnO nanoparticles by Williamson–Hall and size–strain plot methods, Solid State Sci. 13 (2011) 251–256, https://doi.org/10.1016/j.solidstatesciences.2010.11.024.

[39] R.F. Zhuo, H.T. Feng, Q. Liang, J.Z. Liu, J.T. Chen, D. Yan, J.J. Feng, H.J. Li, S. Cheng, B.S. Geng, X.Y. Xu, J. Wang, Z.G. Wu, P.X. Yan, G.H. Yue, Morphology-controlled synthesis, growth mechanism, optical and microwave absorption properties of ZnO nanocombs, J. Phys. D: Appl. Phys. 41 (2008) 185405, https://doi.org/10.1088/0022-3727/41/18/185405.

[40] R. Pagano, C. Ingrosso, G. Giancane, L. Valli, S. Bettini, Wet Synthesis of Elongated Hexagonal ZnO Microstructures for Applications as Photo-Piezoelectric Catalysts, Materials 13 (2020) 2938, https://doi.org/10.3390/ma13132938.

[41] A.N. Kislov, A.F. Zatsepin, Structural and vibrational properties of wurtzite ZnO with oxygen-deficient defects: *ab initio* and potential-based calculations, Phys. Chem. Chem. Phys. 25 (2023) 16354–16362, https://doi.org/10.1039/D3CP01383A.

[42] E. Nowak, M. Szybowicz, A. Stachowiak, W. Koczorowski, D. Schulz, K. Paprocki, K. Fabisiak, S. Los, A comprehensive study of structural and optical properties of ZnO bulk crystals and polycrystalline films grown by sol-gel method, Appl. Phys. A 126 (2020) 552, https://doi.org/10.1007/s00339-020-03711-2.

[43] N. Ben Moussa, M. Lajnef, N. Jebari, C. Villebasse, F. Bayle, J. Chaste, A. Madouri, R. Chtourou, E. Herth, Synthesis of ZnO sol–gel thin-films CMOS-Compatible, RSC Adv. 11 (2021) 22723–22733, https://doi.org/10.1039/D1RA02241E.

[44] U. Haboeck, A. Hoffmann, C. Thomsen, A. Zeuner, B.K. Meyer, High-energy vibrational modes in nitrogen-doped ZnO, Phys. Status Solidi (b) 242 (2005), https://doi.org/10.1002/pssb.200409089.

[45] J. Liu, J. Cao, Z. Li, G. Ji, M. Zheng, A simple microwave-assisted decomposing route for synthesis of ZnO nanorods in the presence of PEG400, Mater. Lett. 61 (2007) 4409–4411, https://doi.org/10.1016/j.matlet.2007.02.014.

[46] Q. Sun, J. Li, Z. Yan, X. Zhang, T. Le, Facile synthesis of zinc oxide crystal and insight into its morphological effect on organic dye photodegradation in water, Appl. Nanosci. 9 (2019) 93–103, https://doi.org/10.1007/s13204-018-0898-2.

[47] G. Schulze, F. Jona, G. Shirane, Ferroelectric Crystals. 402 S. Oxford/London/New York/Paris 1962. Pergamon Press. Preis geb. 84 s net, 512–512, Z. Angew. Math. Und Mech. 43 (1963), https://doi.org/10.1002/zamm.19630431016.
[48] A. Jalalian, A.M. Grishin, X.L. Wang, Z.X. Cheng, S.X. Dou, Large piezoelectric coefficient and ferroelectric nanodomain switching in Ba(Ti0.80Zr0.20)O3-0.5 (Ba0.70Ca0.30)TiO3 nanofibers and thin films, Appl. Phys. Lett. 104 (2014) 103112, https://doi.org/10.1063/1.4867013.
[49] A. Roberts, R. Romanofsky, Implementing a piezoelectric transformer for a ferroelectric phase shifter circuit, Integr. Ferroelectr. 134 (2012) 102–110, https://doi.org/10.1080/10584587.2012.665306.
[50] L. Ye, X. Zhu, Y. Liu, Numerical study on dual-frequency ultrasonic enhancing cavitation effect based on bubble dynamic evolution, Ultrason. Sonochem. 59 (2019) 104744, https://doi.org/10.1016/j.ultsonch.2019.104744.
[51] A.P. Godoy, P. Ecorchard, H. Beneš, J. Tolasz, D. Smržová, L. Seixas, J.J. Pedrotti, E.A.T. de Souza, O.A. El Seoud, R.K. Donato, Ultrasound exfoliation of graphite in biphasic liquid systems containing ionic liquids: a study on the conditions for obtaining large few-layers graphene, Ultrason. Sonochem. 55 (2019) 279–288, https://doi.org/10.1016/j.ultsonch.2019.01.016.
[52] K.H. Chu, Y.A.J. Al-Hamadani, C.M. Park, G. Lee, M. Jang, A. Jang, N. Her, A. Son, Y. Yoon, Ultrasonic treatment of endocrine disrupting compounds, pharmaceuticals, and personal care products in water: A review, Chem. Eng. J. 327 (2017) 629–647, https://doi.org/10.1016/j.cej.2017.06.137.
[53] N. Zhang, G. Zhang, S. Chong, H. Zhao, T. Huang, J. Zhu, Ultrasonic impregnation of MnO2/CeO2 and its application in catalytic sono-degradation of methyl orange, J. Environ. Manag. 205 (2018) 134–141, https://doi.org/10.1016/j.jenvman.2017.09.073.
[54] R. Pagano, S. Bettini, M. Ottolini, G. Ciccarella, L. Valli, G. Giancane, Piezo- and photo- responsive ZnO nanostructures for efficient tetracycline water remediation, Colloids Surf. A: Physicochem. Eng. Asp. 680 (2024) 132626, https://doi.org/10.1016/j.colsurfa.2023.132626.
[55] Z.M. Abou-Gamra, M.A. Ahmed, Synthesis of mesoporous TiO2–curcumin nanoparticles for photocatalytic degradation of methylene blue dye, J. Photochem. Photobiol. B: Biol. 160 (2016) 134–141, https://doi.org/10.1016/j.jphotobiol.2016.03.054.
[56] J. Luo, Z. Niu, Jet and Shock Wave from Collapse of Two Cavitation Bubbles, Sci. Rep. 9 (2019) 1352, https://doi.org/10.1038/s41598-018-37868-x.
[57] K. Sivula, F. LeFormal, M. Grätzel, Solar Water Splitting: Progress Using Hematite (α-Fe $_2$ O $_3$) Photoelectrodes, ChemSusChem 4 (2011) 432–449, https://doi.org/10.1002/cssc.201000416.
[58] H. Shaukat, A. Ali, S. Bibi, S. Mehmood, W.A. Altabey, M. Noori, S.A. Kouritem, Piezoelectric materials: advanced applications in electro-chemical processes, Energy Rep. 9 (2023) 4306–4324, https://doi.org/10.1016/j.egyr.2023.03.077.
[59] T.N. Nhan Nguyen, K.-S. Chang, Piezoelectricity-enhanced multifunctional applications of hydrothermally-grown p-BiFeO3–n-ZnO heterojunction films, Renew. Energy 197 (2022) 89–100, https://doi.org/10.1016/j.renene.2022.07.095.
[60] D. Kumar, S. Sharma, N. Khare, Piezo-phototronic and plasmonic effect coupled Ag-NaNbO3 nanocomposite for enhanced photocatalytic and photoelectrochemical water splitting activity, Renew. Energy 163 (2021) 1569–1579, https://doi.org/10.1016/j.renene.2020.09.132.
[61] S. Li, X. Zhang, F. Yang, J. Zhang, W. Shi, F. Rosei, Mechanically driven water splitting over piezoelectric nanomaterials, Chem. Catal. (2024) 100901, https://doi.org/10.1016/j.checat.2024.100901.